

# Drift-Kinetic Modeling of Particle Acceleration and Transport in Solar Flares

T. Minoshima,<sup>1</sup> S. Masuda, and Y. Miyoshi

*Solar-Terrestrial Environment Laboratory, Nagoya University, Furo-cho, Chikusa-ku,  
Nagoya 464-8601, Japan;*

minoshim@stelab.nagoya-u.ac.jp

## ABSTRACT

Based on the drift-kinetic theory, we develop a model for particle acceleration and transport in solar flares. The model describes the evolution of the particle distribution function by means of a numerical simulation of the drift-kinetic Vlasov equation, which allows us to directly compare simulation results with observations within an actual parameter range of the solar corona. Using this model, we investigate the time evolution of the electron distribution in a flaring region. The simulation identifies two dominant mechanisms of electron acceleration. One is the betatron acceleration at the top of closed loops, which enhances the electron velocity perpendicular to the magnetic field line. The other is the inertia drift acceleration in open magnetic field lines, which produces antisunward electrons. The resulting velocity space distribution significantly deviates from an isotropic distribution. The former acceleration can be a generation mechanism of electrons that radiate loop-top nonthermal emissions, and the latter be of escaping electrons from the Sun that should be observed by *in-situ* measurements in interplanetary space and resulting radio bursts through plasma instabilities.

*Subject headings:* acceleration of particles — plasmas — Sun: flares

## 1. Introduction

Many observations with such as hard X-rays (HXR),  $\gamma$ -rays, and microwaves have revealed that a solar flare is one of the strongest particle accelerator in our solar system.

---

<sup>1</sup>Current address: Institute for Research on Earth Evolution, Japan Agency for Marine-Earth Science and Technology, 3173-25, Syowa-machi, Kanazawaku, Yokohama 236-0001, Japan

Electrons that are accelerated to several tens of keV to MeV radiate HXR at footpoints of flare loops (e.g., Sakao 1994; Krucker et al. 2003; Minoshima et al. 2009), and sometimes above the top of a soft X-ray loop (Masuda et al. 1994, 1995). They are also observed via microwaves in the gigahertz band. These emissions have been used to understand the properties of accelerated electrons (e.g., Nakajima et al. 1983; Kosugi et al. 1988; Silva et al. 2000; Kundu et al. 2001; White et al. 2002; Minoshima et al. 2008). Recently, accelerated ions have been studied by the  $\gamma$ -ray observations of the *Reuven Ramaty High Energy Solar Spectroscopic Imager* (*RHESSI*; Lin et al. 2003; Hurford et al. 2006).

In addition to these observations of accelerated particles at flare sites, escaping particles from the Sun into interplanetary space, the so-called solar energetic particles (SEPs), and resulting radio bursts are observed in association with flares (e.g., Lin et al. 1982; Lin 1985; Ergun et al. 1998; Reames 1999; Krucker et al. 1999, 2007, 2009). Krucker et al. (2007, 2009) have reported detailed examinations of the relationship of electrons between at the flare site and in interplanetary space, by using *RHESSI* and *WIND* observations. On the other hand, escaping electrons are often observed with no corresponding flare activity (e.g., Potter et al. 1980; Gosling et al. 2003; Morioka et al. 2007; Eastwood et al. 2010). This indicates that small-scale particle accelerations frequently take place in the corona.

Based on the magnetic reconnection scenario (Shibata et al. 1995), many authors have proposed models to explain the particle acceleration in solar flares. The particle acceleration in and near the reconnection region has been well discussed. For example, Litvinenko (1996) has studied the DC electric field acceleration in reconnecting current sheets. Hoshino et al. (2001) have discussed the nonadiabatic acceleration in the vicinity of the reconnection region at which the gyro radius is comparable to the curvature radius of the magnetic field line. Fermi acceleration by the contraction of magnetic islands has been studied by Drake et al. (2006). In addition to the acceleration near the reconnection region, stochastic acceleration mechanisms in the reconnection downstream region have been proposed by e.g., Miller et al. (1996) (fast-mode magnetohydrodynamic waves) and Tsuneta & Naito (1998) (oblique shocks), although necessary high-frequency waves for the particle scattering is poorly known in the solar circumstance.

The models greatly contribute to the understanding of how particles are accelerated to observed energies. For the complete understanding of many observed features, however, we should take into account the particle transport and dissipation processes as well as the acceleration in a realistic environment of the solar corona. This is because observed quantities do not necessarily reflect the particle distribution just at the acceleration site, but are the convolution of all of these processes (Aschwanden 1998).

Somov & Kosugi (1997) have proposed a model called “collapsing trap”, in which the

particle acceleration, transport, and dissipation naturally follow from the shrinkage of magnetic loops driven by reconnection. These processes are almost adiabatic in the trap, because the particle gyro scale ( $\sim 10^{-9}$  s and  $\sim 10^0$  cm for electrons) is much smaller than the flare scale ( $\sim 10^2$  s and  $\sim 10^9$  cm) due to very strong magnetic fields in the corona. The adiabatic acceleration may take place everywhere in the trap, which diminishes a serious problem that the number of accelerated particles required for observed HXR intensities is comparable to the number in a whole flare region (Kane 1974; Miller et al. 1997). The mechanism can be regarded as the subsequent acceleration process that occurs after the acceleration near the reconnection region, and as the co-existing process with the acceleration in the downstream region. It is noteworthy to note that the model is very similar to the “dipolarization” associated with substorms in the terrestrial magnetosphere.

In the collapsing trap, particles can adiabatically gain energy from convection electric fields  $\mathbf{E} = -\mathbf{v} \times \mathbf{B}$  through  $\nabla B$  and inertia drift motions. Karlický & Kosugi (2004) have studied the electron distribution function in the shrinking loop, with considering only the acceleration due to the  $\nabla B$  drift (the betatron acceleration). Aschwanden (2004) has analytically considered the electron transport and the resulting impulsive HXR emissions in the loop. Giuliani et al. (2005) have presented a rigorous treatment of the adiabatic motion of a single particle in the loop, by numerically solving guiding-center equations of motion. Karlický & Bárta (2006) have performed a guiding-center test particle simulation in a cusp-shaped loop obtained from a magnetohydrodynamic (MHD) simulation. However, a complete modeling of the evolution of the adiabatic particle distribution in a flare region has not been studied yet.

The correlation between the intensity of HXRs and the strength of convection electric fields has been reported by e.g., Qiu et al. (2002) and Asai et al. (2003, 2004). Recently, Liu et al. (2008) have observed the correlation between the hardness of the HXR spectrum and the strength of convection electric fields along flare ribbons. These observations indicate that the electric field greatly influences the distribution of electrons during their travel in the corona. The adiabatic model with actual coronal parameters can be tested through a direct comparison with these observations, because the model simultaneously describes particle acceleration, transport, and dissipation processes in a very wide area of the corona where particles are strongly magnetized.

To understand the particle acceleration, transport, and dissipation processes in solar flares, we theoretically study the evolution of the particle distribution based on the numerical simulation. For this purpose, we newly develop a comprehensive model based on the drift-kinetic theory, in which the evolution of the particle distribution function is described by means of a numerical simulation of the drift-kinetic Vlasov equation. The simulation can

be performed with actual coronal parameters, allowing us to directly compare it with observations. In § 2 we describe equations of particles and electromagnetic fields in our model. Simulation results are shown in § 3. The simulation identifies two dominant mechanisms of electron acceleration; the betatron acceleration at the top of closed loops and the inertia drift acceleration in open magnetic field lines. We discuss the results in § 4, and then conclude the paper in § 5.

## 2. Models

The evolution of a collisionless plasma is fully described with the Vlasov equation in six-dimensional phase space (three dimensions in the configuration and velocity spaces). The equation describes the full kinetics of the particle transport along and across magnetic field lines, acceleration by electric fields, and the gyromotion, thus can resolve the inertia and gyro scales of particles. When the typical scale of interest is much larger than the gyro scale, it is rather convenient for focusing on the macroscopic distribution of particles to adopt a guiding-center equation (drift kinetics) than the full kinetic equation. In this paper we treat the drift-kinetic Vlasov equation to study the time evolution of the particle distribution function following a macroscopic change of ambient fields.

### 2.1. Basic Equations

We begin with the relativistic guiding-center equations of motion (Northrop 1963),

$$\frac{d\mathbf{r}}{dt} = \mathbf{v} = \frac{u_{\parallel}}{\gamma} \mathbf{b} + \mathbf{v}_d, \quad (1)$$

$$\frac{du_{\parallel}}{dt} = \gamma \mathbf{v}_E \cdot \frac{d\mathbf{b}}{dt} - \frac{M}{\gamma} \frac{\partial B}{\partial s} + \frac{e}{m_0} E_{\parallel}, \quad (2)$$

$$\frac{dM}{dt} = 0, \quad (3)$$

$$\mathbf{v}_d = \mathbf{v}_E + \frac{MB}{\gamma\omega_0} \mathbf{b} \times \nabla \ln B + \frac{1}{\omega_0} \mathbf{b} \times \left( u_{\parallel} \frac{d\mathbf{b}}{dt} + \gamma \frac{d\mathbf{v}_E}{dt} \right), \quad (4)$$

where  $(\mathbf{r}, \mathbf{v})$  is the guiding-center position and velocity of an individual particle,  $\mathbf{v}_d$  is the drift velocity perpendicular to the magnetic field line,  $e$  and  $m_0$  are the charge and rest mass of a particle,

$$\mathbf{b} = \frac{\mathbf{B}}{B}, \quad \mathbf{v}_E = c \frac{\mathbf{E}}{B} \times \mathbf{b}, \quad E_{\parallel} = \mathbf{E} \cdot \mathbf{b},$$

$$\begin{aligned}\mathbf{u} &= \gamma \mathbf{v}, \quad u_{\parallel} = \mathbf{u} \cdot \mathbf{b}, \quad \mathbf{u}_{\perp} = \mathbf{u} - u_{\parallel} \mathbf{b}, \\ \gamma &= \sqrt{(u/c)^2 + 1}, \quad \omega_0 = \frac{eB}{m_0 c}, \quad M = \frac{u_{\perp}^2}{2B}, \\ \frac{d}{dt} &= \frac{\partial}{\partial t} + \frac{u_{\parallel}}{\gamma} \frac{\partial}{\partial s} + (\mathbf{v}_E \cdot \nabla), \quad \frac{\partial}{\partial s} = \mathbf{b} \cdot \nabla,\end{aligned}$$

and  $v_d$  is assumed to be much slower than the speed of light  $c$ . In the drift-kinetic theory, dependent variables are reduced to  $(\mathbf{r}, u_{\parallel}, M)$  by the assumption of gyrotropy. In addition,  $M$  is no longer a variable because of the conservation of the magnetic moment (eq. (3)).

Since observable quantities are the energy and pitch-angle distribution of accelerated particles in the case of solar flares, we convert the variables  $(u_{\parallel}, M)$  into  $(\gamma, \mu)$ , where  $\mu = (\mathbf{v} \cdot \mathbf{b})/v$  is the pitch-angle cosine of a particle. Their time derivatives are written as

$$\frac{d\gamma}{dt} = \omega_0 \frac{\mathbf{v}_d \cdot \mathbf{E}}{cB} + \frac{MB}{\gamma c^2} \frac{\partial \ln B}{\partial t}, \quad (5)$$

$$\frac{d\mu}{dt} = \frac{d}{dt} \left( \frac{u_{\parallel}}{u} \right) = \frac{1}{c\sqrt{\gamma^2 - 1}} \frac{du_{\parallel}}{dt} - \frac{\mu\gamma}{\gamma^2 - 1} \frac{d\gamma}{dt}, \quad (6)$$

where we assume  $E_{\parallel} = 0$ . Using equations (2) and (4), equations (5) and (6) are rewritten as

$$\begin{aligned}\frac{d\gamma}{dt} &= \sqrt{\gamma^2 - 1} \left[ \frac{(1 - \mu^2) \sqrt{\gamma^2 - 1}}{2\gamma} \left( \frac{\partial}{\partial t} + \mathbf{v}_E \cdot \nabla \right) \ln B \right. \\ &\quad \left. + \mu \frac{\mathbf{v}_E}{c} \cdot \left( \frac{\partial}{\partial t} + \frac{\mu c \sqrt{\gamma^2 - 1}}{\gamma} \frac{\partial}{\partial s} + \mathbf{v}_E \cdot \nabla \right) \mathbf{b} \right], \quad (7)\end{aligned}$$

$$\begin{aligned}\frac{d\mu}{dt} &= (1 - \mu^2) \left[ -\frac{\mu}{2} \left( \frac{\partial}{\partial t} + \mathbf{v}_E \cdot \nabla \right) \ln B \right. \\ &\quad \left. + \frac{\gamma}{\sqrt{\gamma^2 - 1}} \frac{\mathbf{v}_E}{c} \cdot \left( \frac{\partial}{\partial t} + \frac{\mu c \sqrt{\gamma^2 - 1}}{\gamma} \frac{\partial}{\partial s} + \mathbf{v}_E \cdot \nabla \right) \mathbf{b} \right. \\ &\quad \left. - \frac{1}{2} \frac{c \sqrt{\gamma^2 - 1}}{\gamma} \frac{\partial \ln B}{\partial s} \right]. \quad (8)\end{aligned}$$

The first term of the equations represents the betatron ( $\nabla B$  drift) force, and the second term is the inertia drift (general form of the curvature drift in the presence of electric fields) force, respectively. The third term of equation (8) is the magnetic mirror force. The polarization drift ( $d\mathbf{v}_E/dt$  in eq. (4)) is negligible by the assumption  $v_E/c \ll 1$ .

The time derivative of the position (eq. (1)) is expressed by the parallel and perpendicular drift motions to the magnetic field line. The drift motion consists of the  $\mathbf{E} \times \mathbf{B}$  drift  $\mathbf{v}_E$ ,  $\nabla B$  drift, inertia drift, and polarization drift (eq. (4)). We estimate these drift velocities in a typical coronal condition. The  $\mathbf{E} \times \mathbf{B}$  drift is a motion of fluid described by MHD, up to an Alfvén velocity  $\sim 2000 \text{ km s}^{-1}$ . The  $\nabla B$  and inertia drifts are  $\sim (r_g/L) v$ , where  $r_g \sim 10^0 \text{ cm}$  is the gyroradius and  $L \sim 10^9 \text{ cm}$  is the characteristic scale of magnetic fields. These are much slower than the Alfvén velocity. The polarization drift is further slower than these drifts. Therefore equation (1) can be well approximated into

$$\frac{d\mathbf{r}}{dt} = \frac{\mu c \sqrt{\gamma^2 - 1}}{\gamma} \mathbf{b} + \mathbf{v}_E. \quad (9)$$

Equations (7) - (9) describe the motion of a particle with the guiding-center variables  $(\mathbf{r}, \gamma, \mu)$ .

We define the particle distribution function  $f(\mathbf{r}, \gamma, \mu) = dN / (d\mathbf{r}d\gamma d\mu)$ , where  $dN$  is the number of particles with  $(\gamma, \mu)$ , and  $d\mathbf{r}d\gamma d\mu$  is the volume element in the phase space. Its time evolution is described by the following continuity equation of the phase space density (the drift-kinetic Vlasov equation; e.g., Wimmel 1984; Gurnett & Bhattacharjee 2005),

$$\frac{\partial f}{\partial t} + \nabla \cdot \left( \frac{d\mathbf{r}}{dt} f \right) + \frac{\partial}{\partial \mu} \left( \frac{d\mu}{dt} f \right) + \frac{\partial}{\partial \gamma} \left( \frac{d\gamma}{dt} f \right) = 0. \quad (10)$$

## 2.2. Electromagnetic Fields

Equation (10) traces the orbit of the particle distribution function in ambient fields. For the determination of the fields, we employ the analytic model of two-dimensional magnetic fields of the flare proposed by Lin et al. (1995). Their model is a superposition of potential and horizontal fields to impose an X-type neutral line at  $(x, z) = (0, a)$ ,

$$A_y(x, z) = \left[ \frac{z + d}{x^2 + (z + d)^2} + \frac{z}{(a + d)^2} \right], \quad (11)$$

$$B_x(x, z) = -\frac{\partial A_y}{\partial z} = -\left[ \frac{x^2 - (z + d)^2}{\{x^2 + (z + d)^2\}^2} + \frac{1}{(a + d)^2} \right], \quad (12)$$

$$B_z(x, z) = \frac{\partial A_y}{\partial x} = -\frac{2x(z + d)}{\{x^2 + (z + d)^2\}^2}, \quad (13)$$

where  $d$  is the depth of a dipole moment. The  $x$ - and  $z$ -axes correspond to the tangential and normal directions relative to the solar surface, and the  $y$ -axis is along the neutral line,

respectively. Note that the above formulae are slightly different from the original ones, because we take the origin at the surface whereas Lin et al. took it at the neutral line.

We introduce an  $x$ -position of the footpoint of the magnetic separatrix  $x_f$ , which is magnetically connected to the neutral line. The relation  $A_y(0, a) = A_y(x_f, 0)$  yields

$$\frac{a}{d} = \left( \frac{x_f}{d} + \sqrt{\left(\frac{x_f}{d}\right)^2 + 1} \right) \frac{x_f}{d}. \quad (14)$$

We further introduce an aspect ratio of the magnetic field configuration  $R = a/x_f$ , which yields

$$\frac{x_f}{d} = \frac{R^2 - 1}{2R}. \quad (15)$$

The geometry of the magnetic field is expressed as a function of  $R$ , which is treated as one of our simulation parameters. Observationally, Aschwanden et al. (1996a,b) have statistically estimated the ratio between the height of the acceleration site and the half length of the footpoint distance from a time-of-flight analysis to HXR data, giving  $1.7 \pm 0.4$ . The magnetic field configuration with  $R = 1.7$  is shown in Figure 1.

The flare evolution can be characterized by the temporal change of the magnetic field configuration. Flares frequently show a separating motion of ribbons in wavelengths sensitive to the chromosphere such as H $\alpha$  (e.g., Qiu et al. 2002; Asai et al. 2003, 2004; Minoshima et al. 2009). Based on the magnetic reconnection model, it is interpreted as a chromospheric counterpart of the rising motion of the neutral line. Tsuneta et al. (1992) reported a growth of a cusp-shaped loop, increasing its height with time. To include the evolution in our simulation, we change the footpoint position of the magnetic separatrix with time. The time derivative (apparent velocity) of the footpoint position is given as a Gaussian profile,

$$\frac{dx_f}{dt} = v_p \exp \left[ -\frac{1}{2} \left( \frac{t - t_p}{\tau} \right)^2 \right]. \quad (16)$$

From equations (14) and (15),  $a$  and  $R$  also change with time.

The temporal change of magnetic fields induces electric fields. Since the electrostatic potential can be assumed to be zero in the two-dimensional system, the  $y$ -component of the electric field is determined from the Faraday's law,

$$\begin{aligned} E_y &= -\frac{1}{c} \frac{\partial A_y}{\partial t} = -\frac{1}{c} \frac{dx_f}{dt} \frac{\partial a}{\partial x_f} \frac{\partial A_y}{\partial a} \\ &= \left[ \frac{2x_f}{d} + \frac{2(x_f/d)^2 + 1}{\sqrt{(x_f/d)^2 + 1}} \right] \frac{2z}{(a+d)^3} \frac{1}{c} \frac{dx_f}{dt}, \end{aligned} \quad (17)$$

and other components are zero. The model electric field is a linear function of  $z$ , taking zero at the surface. This means that the magnetic field lines at the surface are stationary. Since the electric field is proportional to  $dx_f/dt$ , the strength grows till  $t = t_p$  (we call the period as the rising phase), and then is reduced (the declining phase).

### 2.3. Simulation Setup

Using the listed equations, we numerically solve the drift-kinetic Vlasov equation (10). Since we assume two-dimensionality in the configuration space, the equation is reduced to a four-dimensional compressive advection equation. To solve it, we adopt the R-CIP-CSL2 scheme with operator splitting technique (Nakamura et al. 2001), which simultaneously solves the integrated values of  $f$  as well as  $f$  itself to keep “subgrid” information and to satisfy mass conservation.

Simulation parameters are  $d = 1.5 \times 10^9$  cm and  $R(t = 0) = 1.7$ . Considering that the position of flare ribbons corresponds to the root of the magnetic separatrix, we set the parameters in equation (16) based on observations. Qiu et al. (2002) have observed the apparent motion of flare kernels seen in the  $H\alpha$  line. The velocity reaches several ten to 100 km s<sup>-1</sup> within a time scale of  $\sim 10$  s (see Figs. 5 and 6 in their paper). Referring to the first spike in Figure 5(b) of Qiu et al., we set  $v_p = 60$  km s<sup>-1</sup>,  $\tau = 1.77$  s, and  $t_p = 5.0$  s. The simulation runs till  $t = 10$  s. Length  $(x, z, a, x_f)$  is normalized to  $d$ .

We limit a calculation domain of the configuration space to the area below the dash-dotted line in Figure 1, in which the  $\mathbf{E} \times \mathbf{B}$  drift velocity calculated with equations (12), (13), and (17) does not exceed a typical Alfvén velocity in the corona ( $\sim 2000$  km s<sup>-1</sup>). In other word, our model can not properly describe the electric field around the neutral line, where the  $\mathbf{E} \times \mathbf{B}$  drift velocity is calculated to be an unrealistic value. Figure 2 shows an example of the  $\mathbf{E} \times \mathbf{B}$  drift velocity field distribution within the simulation domain.

Initially, 3 keV isotropic electrons are uniformly distributed in the configuration space. We will discuss the assumption of the relatively high initial temperature in § 4. The initial uniform distribution is reasonable, because the hydrostatic scale height is much longer than the size of the simulation domain. At  $x = x_{\max}$  and  $z = z_{\max}$  we impose the open boundary condition where incoming fluxes are assumed while outgoing fluxes are perfectly lost. The incoming flux is fixed to the initial distribution. We also impose another open boundary condition at  $z = 0$ , where a cold dense plasma is fixed to exclude the possibility of hot electrons originating below the surface. The boundary condition at  $x = 0$  is symmetric:  $f(x, z, \gamma, \mu) = f(-x, z, \gamma, -\mu)$ . We note that the initial uniform and isotropic distribution



is not a steady state solution in our model, because of the different boundary conditions at  $z = z_{\max}$  (hot tenuous plasma) and  $z = 0$  (cold dense plasma).

We use  $64 \times 96$  cells in  $(x, z)$  space, and  $64 \times 64$  cells in  $(\gamma, \mu)$  space. A domain of  $\gamma$  is 1.01-1.20, corresponding to 0.511-102.2 keV electrons. The grids in  $\gamma$  space are logarithmically spaced.

### 3. Simulation Results and Interpretation

Several snapshots of our simulation results are in Figure 3, in which the spatial distributions of the number of 20 keV and 50 keV omnidirectional electrons at  $t = 5$  s and 10 s are presented. In both energies the electron number increases significantly around the top of closed loops. The altitude of the peak position of the electron number decreases with time, due to the shrinkage of the loops. The distributions in the loops diffuse along the magnetic field lines. The spatial diffusion is more prominent for lower energy electrons. Because of the boundary condition at  $z = 0$ , the number of electrons decreases at the bottom area.

#### 3.1. Electron Distribution in Closed Loops

As seen in Figure 3, a strong acceleration takes place around the loop top, at which the fastest  $\mathbf{E} \times \mathbf{B}$  drift velocity is observed (see Fig. 2). The velocity space distribution is of help to understand the mechanism around there. Figure 4 shows the velocity space distribution function taken at the loop top  $(x, z) = (0, 0.7)$  at  $t = 10$  s. The horizontal and vertical axes correspond to the velocity parallel and perpendicular to the magnetic field line.

The distribution significantly deviates from the initial, isotropic Maxwell distribution. It shows the loss-cone distribution with a loss-cone angle (white lines) defined as  $\alpha = \sin^{-1} \sqrt{B(x, z)/B(x_{FP}, 0)}$ , where  $x_{FP}$  is the  $x$ -position at the footpoint of a specific field line determined from  $A_y(x_{FP}, 0) = A_y(x, z)$ . The distribution also shows a strong enhancement of the number of electrons perpendicular to the field line. The perpendicular enhancement is energy dependent; the distribution is more anisotropic for higher energy electrons. This means that high energy electrons are produced by the acceleration perpendicular to the field line, that is, the betatron ( $\nabla B$  drift) acceleration. Since the electron pitch angle becomes close to 90 degrees by the betatron acceleration, accelerated electrons are further confined and energized at the loop top with time.

By taking the second-order momentum of the distribution function, we estimate the

average energies (temperatures) parallel and perpendicular to the magnetic field line as

$$T_{\parallel}(x, z, t) = \int_1^{\infty} d\gamma \int_{-1}^1 d\mu \frac{u_{\parallel}^2}{\gamma} f, \quad (18)$$

$$T_{\perp}(x, z, t) = \frac{1}{2} \int_1^{\infty} d\gamma \int_{-1}^1 d\mu \frac{u_{\perp}^2}{\gamma} f, \quad (19)$$

where  $u_{\parallel}^2 = \mu^2 (\gamma^2 - 1)$  and  $u_{\perp}^2 = (1 - \mu^2) (\gamma^2 - 1)$ . The spatial distributions of the parallel and perpendicular temperatures at  $t = 5$  s and 10 s are shown in Figure 5. Around the loop top, we can see a slight decrease of the parallel temperature and a strong increase of the perpendicular temperature relative to an initial temperature 3 keV. The decrease of the parallel temperature is due to the loss of electrons inside the loss cone. The perpendicular temperature reaches a maximum  $\sim 15$  keV at  $(x, z) = (0, 0.7)$  at  $t = 10$  s. The acceleration increases the perpendicular temperature by a factor of 5 relative to the initial.

On the other hand, the rate of the betatron acceleration for electrons with  $\mu = 0$  is easily obtained from the conservation of the magnetic moment (eq. (3)),

$$\frac{\epsilon_2}{\epsilon_1} = \frac{B_2}{B_1}, \quad (20)$$

where  $\epsilon = \gamma - 1 (\ll 1)$  is the kinetic energy. Since the loop at  $(x, z) = (0, 0.7)$  at  $t = 10$  s is convected from the initial position  $(x, z) = (0, 0.89)$  by the  $\mathbf{E} \times \mathbf{B}$  drift, a compression ratio at the loop top is

$$\frac{B(t = 10 \text{ s})}{B(t = 0 \text{ s})} \sim \frac{0.0935}{0.0156} = 6, \quad (21)$$

which is larger than the estimated increase rate of the perpendicular temperature. This is because the betatron acceleration less works for electrons with smaller pitch angles. They are accelerated rather parallel to the magnetic field line through the inertia drift.

To consider the acceleration due to the inertia drift in the closed loop, it is convenient to introduce the longitudinal adiabatic invariant,  $u_{\parallel} L = \text{constant}$ . Here  $L$  is the travel length of electrons measured along the field line,

$$L = 2 \int_{\text{loop-top}}^{\text{mirror}} ds = 2 \int_0^{x_{\text{mirror}}} \sqrt{1 + (B_z/B_x)^2} dx, \quad (22)$$

where  $x_{\text{mirror}}$  is the  $x$ -position at the mirror point. For electrons with the pitch angle close enough to the loss-cone angle,  $x_{\text{mirror}} = x_{FP}$ . The inertia drift acceleration in the loop is expressed as the increase of the parallel energy due to the decrease of the length of the shrinking loop. The rate of the inertia drift acceleration is

$$\frac{\epsilon_2}{\epsilon_1} = \left( \frac{L_1}{L_2} \right)^2. \quad (23)$$

By numerically calculating the length of the loop that is initially at  $(x, z) = (0, 0.89)$  (the same loop as in eq. (21)), we obtain

$$\left(\frac{L(t = 0 \text{ s})}{L(t = 10 \text{ s})}\right)^2 \sim \left(\frac{1.076}{0.943}\right)^2 = 1.3. \quad (24)$$

Electrons that experience the inertia drift acceleration escape from the loop top and their distribution diffuses along the field line. This yields the perpendicular temperature that is not as much as expected from the field compression (eq. (21)). Nonetheless, the resulting velocity space distribution is enhanced perpendicular to the field line (Fig. 4), because the rate of the perpendicular acceleration  $\sim 6$  is larger than the parallel  $\sim 1.3$ . This is the general feature of acceleration with conserving both the magnetic moment and longitudinal invariant.

### 3.2. Electron Distribution in Open Field lines

In the previous section, we discussed the acceleration taking place in the closed loop. It is interesting to discuss whether the acceleration occurs also in open field lines. Figure 6 shows the electron pitch-angle distribution in the open field line near the magnetic separatrix at  $(x, z) = (0.14, 0.87)$  at  $t = 5$  s. The positive (negative) value of the pitch-angle cosine corresponds to the sunward (antisunward) direction.

The pitch-angle distribution is different between sunward and antisunward directions. For sunward ( $\mu > 0$ ) the distribution is almost isotropic, because isotropic electrons are continuously injected from the upper boundary. For antisunward ( $\mu < 0$ ), on the other hand, the distribution deviates from an isotropic distribution. We see lack of electrons with  $\mu \sim -1$ , also due to the boundary condition. Since we impose the lower boundary condition as almost vacuum for high energy electrons, the antisunward electrons are composed by those that are injected from the upper boundary (with  $\mu > 0$ ) and then are reflected (change the sign of  $\mu$ ) by the magnetic mirror force. Injected electrons with  $\mu \sim 1$  can not be reflected, and are lost at the lower boundary. Therefore electrons with  $\mu \sim -1$  are not found along open field lines.

We find a slight enhancement of the number of electrons with  $\mu \sim -0.95$  and decrease with  $-0.8 \lesssim \mu < 0$ , compared to those with  $\mu > 0$ . This is an evidence of the parallel acceleration to the magnetic field line due to the inertia drift: Electrons are accelerated antisunward along the curved line by the centrifugal force. This mechanism has been proposed for the generation of energetic particles in the planetary magnetosphere (e.g., Delcourt et al. 1996, 2005), and in quasi-perpendicular shocks (Amano & Hoshino 2007).

According to Amano & Hoshino (2007), we discuss the resulting pitch-angle distribution of this acceleration. In the rest frame, electrons gain energy from convection electric fields through the inertia drift. It is convenient to transform the frame into the so-called de Hoffmann-Teller frame moving with  $\mathbf{v}_E$  relative to the rest frame, in which the electric field vanishes and hence electrons do not gain energy from convection electric fields. In this frame, however, magnetic mirror points move relative to electrons when a magnetic field line has curvature. The velocity of the mirror point measured in the de Hoffmann-Teller frame is

$$\mathbf{v}_{\text{mirror}} = -\mathbf{v}_E \tan \theta, \quad (25)$$

where  $\theta$  is an angle of the magnetic field line between the departure and mirror points of an electron. When  $\mathbf{v}_E$  is sunward in the rest frame, the mirror point moves antisunward in the de Hoffmann-Teller frame. Sunward electrons experience a head-on reflection with the mirror points, which increases the electron parallel velocity by  $2v_{\text{mirror}}$  and changes the direction.

The changes of the electron pitch angle and speed by the reflection are written as

$$\mu' = -\left(\frac{\mu v + 2v_{\text{mirror}}}{v'}\right), \quad (\text{if } \mu > 0), \quad (26)$$

$$(v')^2 = (\mu' v')^2 + (1 - \mu^2)v^2, \quad (27)$$

where variables with (without) a prime are measured after (before) the reflection. The second term of equation (27) is the square of the perpendicular velocity, which remains constant throughout the reflection. The resulting antisunward electron distribution  $f'$  is

$$f'(1 + \epsilon', \mu') = f_{\text{sunward}}(1 + \epsilon, \mu), \quad (\text{if } \mu' < 0), \quad (28)$$

where  $\epsilon = \gamma - 1 \simeq (v/c)^2/2$ . Note that the sunward electron distribution  $f_{\text{sunward}}$  is independent of  $\mu$ ,  $f_{\text{sunward}}(1 + \epsilon, \mu) = f_{\text{sunward}}(1 + \epsilon)$ , because it is an almost isotropic Maxwellian. With equations (26) and (27), equation (28) results in

$$f'(1 + \epsilon', \mu') = f_{\text{sunward}}(1 + \epsilon' + 4\mu'\sqrt{\epsilon'\epsilon_{\text{mirror}}} + 4\epsilon_{\text{mirror}}), \quad (29)$$

where  $\epsilon_{\text{mirror}} = (v_{\text{mirror}}/c)^2/2$ .

To determine  $\epsilon_{\text{mirror}}$ , we suppose that an electron with  $\mu_0 (> 0)$  is initially at  $\mathbf{S}$ , moves sunward, and then is reflected at  $\mathbf{R}$ . The position of the mirror point is determined from the conservation of the magnetic moment,

$$B(\mathbf{R}) = \frac{B(\mathbf{S})}{1 - \cos \mu_0^2}, \quad (30)$$

which depends on the electron initial condition. The velocity of the mirror point (eq. (25)) depends on the electron initial condition as well as the field configuration, which is evaluated as

$$\mathbf{v}_{\text{mirror}} = -\mathbf{v}_E(\mathbf{S}) \tan [\cos^{-1} \{\mathbf{b}(\mathbf{S}) \cdot \mathbf{b}(\mathbf{R})\}]. \quad (31)$$

We need to determine the mirror point of electrons with different pitch angles, to calculate equation (29) with (31).

Using equations (7) - (9), we trace the position of electrons backward in time. Electrons are set at  $(x, z) = (0.14, 0.87)$  at  $t = 5$  s, same as employed in Figure 6. Determining the mirror points from this test particle simulation, we obtain  $\tan \theta$  as a function of the electron initial pitch angle in Figure 7. The velocity of the mirror point certainly depends on the electron initial pitch angle. Using this result, we can calculate the analytic solution of the electron distribution (eq. (29)), which is presented in Figure 8. The solution shows an enhancement of the number of electrons with  $\mu \sim -0.95$ , similar to the simulation (Fig. 6). This confirms that the simulation result is certainly interpreted as the above process.

### 3.3. Electron Escape from the Sun

The accelerated electrons due to the inertia drift propagate antisunward along open field lines, reach the upper boundary, and finally escape from the simulation domain. It is important to consider the number of these escaping electrons and their time evolution. Figure 9 shows the time evolution of the spatial distribution of the number of 20 keV antisunward electrons. This figure emphasizes the gradient in open field lines (right-half area), to focus on the escaping electrons.

During the rising phase ( $t = 1 - 5$  s) the number of antisunward electrons decreases (identified as upward-shifting contours), meaning that the number of escaping electrons increases due to the growth of the electric field. The decrease of the electron number is more significant at the higher area, because the electric field is a monotonically increasing function of  $z$ . During the declining phase ( $t = 5 - 9$  s) the number of electrons recovers (identified as downward-shifting contours), because the electric field is reduced while constant electron fluxes are continuously injected from the upper boundary. The electron distribution at  $t = 9$  s is almost same as at  $t = 1$  s, because the electric field distribution is close.

The inertia drift acceleration takes place in a whole area of open field lines, especially near the magnetic separatrix (e.g., Fig. 6). We estimate the number of escaping electrons as

$$f_{\text{escape}}(\gamma, t) = - \iint dx dz \left[ \frac{1}{A(t)} \int_{-1}^0 f(t) d\mu - \frac{1}{A(10 \text{ s})} \int_{-1}^0 f(10 \text{ s}) d\mu \right], \quad (32)$$

where  $A(t)$  is the time-varying area of open field lines in the simulation domain, and the integration over the configuration space is implemented only in the area of open field lines. Here we use  $f(10\text{ s})$  as a reference, not the initial distribution  $f(0\text{ s})$ , because the initial distribution is not a steady state solution in our model (see § 2.3). Figure 10 shows the time profile of the number of 20 keV escaping electrons. The solid line is obtained from the usual simulation result. The dashed line is from the result with the apparent velocity of the footpoint  $v_p = 30\text{ km s}^{-1}$ , which is a half relative to the usual.

The time profile of the escaping electrons is similar to that of the apparent velocity of the footpoint, and thus the electric field (eqs. (16) and (17)). This is understood as follows. A travel time of the escaping electrons in open field lines is  $\lesssim 1\text{ s}$ , which is much faster than the time scale of the temporal change of the electric field. The accelerated electrons instantaneously reach the upper boundary and escape without being influenced by the temporal change of the electric field. Therefore the escaping electrons should directly reflect the instantaneous configuration of the electric field.

The maximum number of the 20 keV escaping electrons is  $\sim 1\%$  of the initial. We confirm the similar percentage at maximum in 10 - 50 keV. For electrons below 10 keV, the number is slightly small,  $\sim 0.3\%$ . Comparing the solid and dashed lines, it is found that the number of the escaping electrons is proportional to the electric field strength. As discussed, the rate of the inertia drift acceleration is simply proportional to the electric field ( $v_{\text{mirror}} \propto v_E \propto E$ ) so that it is expected that the number of escaping electrons correlates with the electric field.

#### 4. Discussion

The drift-kinetic simulation has identified two dominant mechanisms of electron acceleration in solar flares. One is the betatron acceleration at the top of closed loops, which enhances the electron velocity perpendicular to the magnetic field line. The other is the inertia drift acceleration in open magnetic field lines, which produces antisunward electrons. The resulting velocity space distribution significantly deviates from an isotropic distribution.

The betatron acceleration yields more confinement of higher energy electrons at the loop top, as previously mentioned in the collapsing trap model (Somov & Kosugi 1997; Karlický & Kosugi 2004; Karlický & Bárta 2006). They can be a candidate for radiating loop-top nonthermal emissions such as “above-the-loop-top” HXR sources (Masuda et al. 1994, 1995) and microwaves (e.g., Kundu et al. 2001; White et al. 2002; Melnikov et al. 2002; Huang & Nakajima 2009). Minoshima et al. (2008) have found that the distribution of elec-

trons is enhanced perpendicular to the field line when they are injected into a loop, from both observations of the 2003 May 29 flare and a numerical modeling of the electron transport with the Fokker-Planck equation. This result can be interpreted that the betatron acceleration is the most dominant mechanism for the electron energization in the flare.

The betatron acceleration at the loop top is quite reasonable to radiate loop-top non-thermal emissions. However, it is widely known that the most of HXR emissions are from footpoints of the loop. This indicates a large amount of electrons precipitating there. In the model almost all of electrons are trapped in the loop. One of the reasons for this discrepancy is that the model has not taken into account the pitch-angle scattering. The pitch-angle scattering leads electrons into the loss cone, and significantly increases the rate of the precipitation. Many authors have argued the effect of the pitch-angle scattering of electrons by the Coulomb collisions with ambient plasma (Melrose & Brown 1976; Aschwanden et al. 1998, 1999; Minoshima et al. 2008). Another agency for the scattering is plasma waves. In particular, we suggest whistler waves as a possible candidate, because the perpendicular temperature anisotropy at the loop top in the simulation (Fig. 5) is unstable for the whistler wave growth. The enhancements of the pitch-angle scattering by the interaction with whistler waves might efficiently work on the precipitation and subsequent HXR emissions at footpoints, similar to the precipitation of radiation belt electrons and diffuse auroral emissions at the Earth. We plan further simulations with including the pitch-angle scattering as diffusion terms in equation (10).

The number of escaping electrons produced by the inertia drift acceleration has been estimated up to  $\sim 1\%$  of the background (Fig. 10). The escaping electrons have been observed in association with flares, and their number is estimated to  $\sim 0.1 - 1\%$  of the observed HXR-emitting electrons precipitating into the chromosphere (e.g., Lin 1974; Krucker et al. 2007). The observed number of escaping electron is expected to be less than  $\sim 1\%$  of the background, because the observed number of HXR-emitting electrons should be less than the background. Therefore our estimation from the simulation can account for observations. The inertia drift acceleration takes place in a whole area of open field lines and contributes this high efficiency, as long as curved magnetic field lines keeps moving. It is noted that the observation can be understood without a complex phenomenon such as magnetic reconnection for the acceleration.

Because of its ubiquity, we suggest the inertia drift acceleration as a possible mechanism for producing escaping electrons that are not always associated with flares (e.g., Potter et al. 1980; Gosling et al. 2003; Morioka et al. 2007; Eastwood et al. 2010). Morioka et al. (2007) have reported the so-called “micro type-III” radio bursts. Micro type-III radio bursts, characterized by short-lived, continuous, and weak emissions, are thought to be an evidence of the

ubiquitous electron acceleration in the solar corona. They have found that the micro type-III radio bursts are observed when the active regions bordering on coronal holes appear. It may suggest that parent electrons are accelerated near the boundary and then escape into interplanetary space. We have shown that antisunward electrons are produced especially near the magnetic separatrix, which qualitatively supports the observational results of Morioka et al. (2007).

In § 3.3 we have discussed that the time profile of the escaping electrons by the inertia drift acceleration reflects that of the electric field, because the travel time of the electrons is faster than the time scale of the temporal change of the electric field. As long as satisfying the condition, it is expected that the time scale of the escaping electrons becomes shorter following more rapid change of the electric field than we have employed ( $\tau = 1.77$  s). It may explain type-III radio bursts that have an elemental time scale shorter than  $\sim 1$  s, while other mechanisms may also contribute to the acceleration. The escaping electrons may further be accelerated at a higher altitude, for example, the vicinity of the reconnection region and the possible turbulent region. The inertia drift acceleration can contribute to supply electrons to the higher corona and the interplanetary space where the secondary acceleration may occur.

Minoshima et al. (2009) have reported that the electron distribution in the loop is enhanced parallel to the field line in the 2006 December 13 flare. They have argued that the distribution could be formed, if the inertia drift acceleration efficiently takes place. Such a distribution has not been formed in our model. In the drift-kinetic model, the betatron and inertia drift accelerations take place simultaneously; the former enhances the velocity distribution in the perpendicular direction while the latter in the parallel. The resulting distribution is determined by combination of these accelerations. We have found in §3.1 that the rate of the betatron acceleration  $\sim 6$  is more efficient than that of the inertia drift  $\sim 1.3$  in the closed loop of the model magnetic field. However, it may be expected that the inertia drift acceleration overcomes the betatron in different field configurations, and it is possible that the resulting electron distribution is enhanced rather parallel to the field line.

Let us simply consider the relationship between the magnetic field configuration of the loop and the distribution of accelerated particles. Suppose that the magnetic field strength at the loop top is proportional to its altitude,  $B \propto z^{-\xi}$ . When the magnetic field is compressed by a factor of  $R_c$ , the altitude decreases by a factor of  $R_c^{1/\xi}$ . We assume that the travel length of particles along the field line  $L$  is proportional to the altitude. From equations (20) and (23), we describe the increase of the perpendicular and parallel energies through the compression as

$$\begin{cases} \epsilon_{\perp}/\epsilon_{\perp,0} = R_c, \\ \epsilon_{\parallel}/\epsilon_{\parallel,0} = R_c^{2/\xi}. \end{cases} \quad (33)$$



It is found that particles are accelerated perpendicular rather than parallel to the magnetic field line when  $\xi > 2$ . Figure 11 shows the local index  $\xi$  of the model magnetic field at the apex of loops ( $x = 0$ ). The index is much larger than 2 at the higher altitude where electrons are more accelerated by stronger electric fields (Fig. 3). This is consistent with the perpendicular enhancement of the electron distribution function around the loop top, shown in Figure 4. Meanwhile, we propose from equation (33) that it may be possible to enhance the particle distribution parallel to the field line when the loop configuration meets  $0 < \xi < 2$ . To verify this hypothesis, we should perform simulations with various field models, e.g., MHD simulation results (Karlický & Bárta 2006), and realistic fields extrapolated from *Hinode* observations (Inoue et al. 2008; Kusano et al. 2008). Toward the understanding of particle acceleration in solar flares through both the observations and simulations, it is critically important to study the relationship between a variety of magnetic field configurations and the resulting particle phase space distribution.

Due to the numerical limitation, we have performed the simulation with a relatively high initial temperature 3 keV. Although the acceleration efficiency is dependent on the temperature, it does not mean that the pre-acceleration is necessary for the proposed acceleration mechanisms. In fact, we have also performed the simulation with an initial temperature 1.5 keV, and obtain similar results. This is to be expected, because the adiabatic betatron acceleration takes place similarly regardless of the particle energy. For the inertia drift acceleration, the particle velocity should be faster than the mirror point velocity to be reflected. Electrons can easily meet this condition. Therefore the acceleration takes place even for electrons with the temperature lower than we have employed in this study.

Let us discuss the effect of the three-dimensionality of ambient fields, for example, the shear motion and/or guiding magnetic fields. In the three-dimensional system, the fields may evolve so as to generate field-aligned currents. The carrier of the current should be electrons, because of their high mobility. If electrons are inhibited to move along the field line by such as the magnetic mirror force and the pressure gradient (acting as a resistivity), parallel electric fields will be generated and accelerate electrons, to carry the current required from the field evolution (e.g., Tsuneta 1995). As a result, their distribution will be significantly modified from the two-dimensional system, particularly in the parallel direction. The concept of the current-voltage relation has been utilized especially for the auroral particle acceleration along the magnetic field line at the Earth (Knight 1973). For the electron acceleration in the three-dimensional system, it may be essential to consider the parallel electric field and the electrostatic potential.

## 5. Conclusion

Based on the drift-kinetic theory, we have developed a comprehensive model for particle acceleration and transport in solar flares. Using this model, we have simulated the time evolution of the electron distribution in a flaring region. There are two dominant mechanisms of electron acceleration. The betatron acceleration takes place at the top of closed loops. It can be a generation mechanism of electrons that radiate loop-top nonthermal emissions. The phase space distribution of accelerated particles in the loop strongly depends on the magnetic field configuration. The inertia drift acceleration also takes place in open magnetic field lines, producing escaping electrons from the Sun. The number of escaping electrons estimated from the simulation can account for the observed number of flare-associated escaping electrons. The inertia drift acceleration is caused by a motion of curved field lines, which is not necessarily driven by magnetic reconnection. In this sense, we propose the acceleration in this study as a mechanism for producing escaping electrons that are not always associated with flares.

We thank to K. Kusano, T. Yokoyama, T. Amano, A. Morioka, and M. J. Aschwanden for fruitful discussions and comments. We also thank to anonymous referee for valuable comments to improve our manuscript. T. M. is supported by the Grant-in-Aid for Young Scientists (B) #21740135 and partly by the Grant-in-Aid for Creative Scientific Research of MEXT/Japan, the Basic Study of Space Weather Predication. This work is a part of the GEMSIS (Geospace Environment Modeling System for Integrated Studies) project of Solar-Terrestrial Environment Laboratory, Nagoya University.

## REFERENCES

- Amano, T., & Hoshino, M. 2007, *ApJ*, 661, 190
- Asai, A., Ishii, T. T., Kurokawa, H., Yokoyama, T., & Shimojo, M. 2003, *ApJ*, 586, 624
- Asai, A., Yokoyama, T., Shimojo, M., Masuda, S., Kurokawa, H., & Shibata, K. 2004, *ApJ*, 611, 557
- Aschwanden, M. J. 1998, *ApJ*, 502, 455
- . 2004, *ApJ*, 608, 554
- Aschwanden, M. J., Fletcher, L., Sakao, T., Kosugi, T., & Hudson, H. 1999, *ApJ*, 517, 977

- Aschwanden, M. J., Kosugi, T., Hudson, H. S., Wills, M. J., & Schwartz, R. A. 1996a, *ApJ*, 470, 1198
- Aschwanden, M. J., Schwartz, R. A., & Dennis, B. R. 1998, *ApJ*, 502, 468
- Aschwanden, M. J., Wills, M. J., Hudson, H. S., Kosugi, T., & Schwartz, R. A. 1996b, *ApJ*, 468, 398
- Delcourt, D. C., Sauvaud, J., Martin, R. F., & Moore, T. E. 1996, *J. Geophys. Res.*, 101, 17409
- Delcourt, D. C., Seki, K., Terada, N., & Miyoshi, Y. 2005, *Annales Geophysicae*, 23, 3389
- Drake, J. F., Swisdak, M., Che, H., & Shay, M. A. 2006, *Nature*, 443, 553
- Eastwood, J. P., et al. 2010, *ApJ*, 708, L95
- Ergun, R. E., et al. 1998, *ApJ*, 503, 435
- Giuliani, P., Neukirch, T., & Wood, P. 2005, *ApJ*, 635, 636
- Gosling, J. T., Skoug, R. M., & McComas, D. J. 2003, *Geophys. Res. Lett.*, 30, 130000
- Gurnett, D. A., & Bhattacharjee, A. 2005, *Introduction to Plasma Physics*, ed. Gurnett, D. A. & Bhattacharjee, A.
- Hoshino, M., Mukai, T., Terasawa, T., & Shinohara, I. 2001, *J. Geophys. Res.*, 106, 25979
- Huang, G., & Nakajima, H. 2009, *ApJ*, 696, 136
- Hurford, G. J., Krucker, S., Lin, R. P., Schwartz, R. A., Share, G. H., & Smith, D. M. 2006, *ApJ*, 644, L93
- Inoue, S., et al. 2008, in *Astronomical Society of the Pacific Conference Series*, Vol. 397, *First Results From Hinode*, ed. S. A. Matthews, J. M. Davis, & L. K. Harra, 110–+
- Kane, S. R. 1974, in *IAU Symp. 57: Coronal Disturbances*, 105–141
- Karlický, M., & Bárta, M. 2006, *ApJ*, 647, 1472
- Karlický, M., & Kosugi, T. 2004, *A&A*, 419, 1159
- Knight, S. 1973, *Planet. Space Sci.*, 21, 741
- Kosugi, T., Dennis, B. R., & Kai, K. 1988, *ApJ*, 324, 1118

- Krucker, S., Hurford, G. J., & Lin, R. P. 2003, *ApJ*, 595, L103
- Krucker, S., Kontar, E. P., Christe, S., & Lin, R. P. 2007, *ApJ*, 663, L109
- Krucker, S., Larson, D. E., Lin, R. P., & Thompson, B. J. 1999, *ApJ*, 519, 864
- Krucker, S., Oakley, P. H., & Lin, R. P. 2009, *ApJ*, 691, 806
- Kundu, M. R., Nindos, A., White, S. M., & Grechnev, V. V. 2001, *ApJ*, 557, 880
- Kusano, K., et al. 2008, AGU Fall Meeting Abstracts, A6+
- Lin, J., Forbes, T. G., Priest, E. R., & Bungey, T. N. 1995, *Sol. Phys.*, 159, 275
- Lin, R. P. 1974, *Space Science Reviews*, 16, 189
- . 1985, *Sol. Phys.*, 100, 537
- Lin, R. P., et al. 2003, *ApJ*, 595, L69
- Lin, R. P., Mewaldt, R. A., & van Hollebeke, M. A. I. 1982, *ApJ*, 253, 949
- Litvinenko, Y. E. 1996, *ApJ*, 462, 997
- Liu, C., Lee, J., Jing, J., Gary, D. E., & Wang, H. 2008, *ApJ*, 672, L69
- Masuda, S., Kosugi, T., Hara, H., Sakao, T., Shibata, K., & Tsuneta, S. 1995, *PASJ*, 47, 677
- Masuda, S., Kosugi, T., Hara, H., Tsuneta, S., & Ogawara, Y. 1994, *Nature*, 371, 495
- Melnikov, V. F., Shibasaki, K., & Reznikova, V. E. 2002, *ApJ*, 580, L185
- Melrose, D. B., & Brown, J. C. 1976, *MNRAS*, 176, 15
- Miller, J. A., et al. 1997, *J. Geophys. Res.*, 102, 14631
- Miller, J. A., Larosa, T. N., & Moore, R. L. 1996, *ApJ*, 461, 445
- Minoshima, T., et al. 2009, *ApJ*, 697, 843
- Minoshima, T., Yokoyama, T., & Mitani, N. 2008, *ApJ*, 673, 598
- Morioka, A., et al. 2007, *ApJ*, 657, 567
- Nakajima, H., Kosugi, T., Kai, K., & Enome, S. 1983, *Nature*, 305, 292

- Nakamura, T., Tanaka, R., Yabe, T., & Takizawa, K. 2001, *Journal of Computational Physics*, 174, 171
- Northrop, T. G. 1963, *Reviews of Geophysics and Space Physics*, 1, 283
- Potter, D. W., Lin, R. P., & Anderson, K. A. 1980, *ApJ*, 236, L97
- Qiu, J., Lee, J., Gary, D. E., & Wang, H. 2002, *ApJ*, 565, 1335
- Reames, D. V. 1999, *Space Science Reviews*, 90, 413
- Sakao, T. 1994, PhD thesis, Univ. Tokyo
- Shibata, K., et al. 1995, *ApJ*, 451, L83+
- Silva, A. V. R., Wang, H., & Gary, D. E. 2000, *ApJ*, 545, 1116
- Somov, B. V., & Kosugi, T. 1997, *ApJ*, 485, 859
- Tsuneta, S. 1995, *PASJ*, 47, 691
- Tsuneta, S., et al. 1992, *PASJ*, 44, L63
- Tsuneta, S., & Naito, T. 1998, *ApJ*, 495, L67
- White, S. M., Kundu, M. R., Garaimov, V. I., Yokoyama, T., & Sato, J. 2002, *ApJ*, 576, 505
- Wimmel, H. K. 1984, *Phys. Scr*, 29, 141

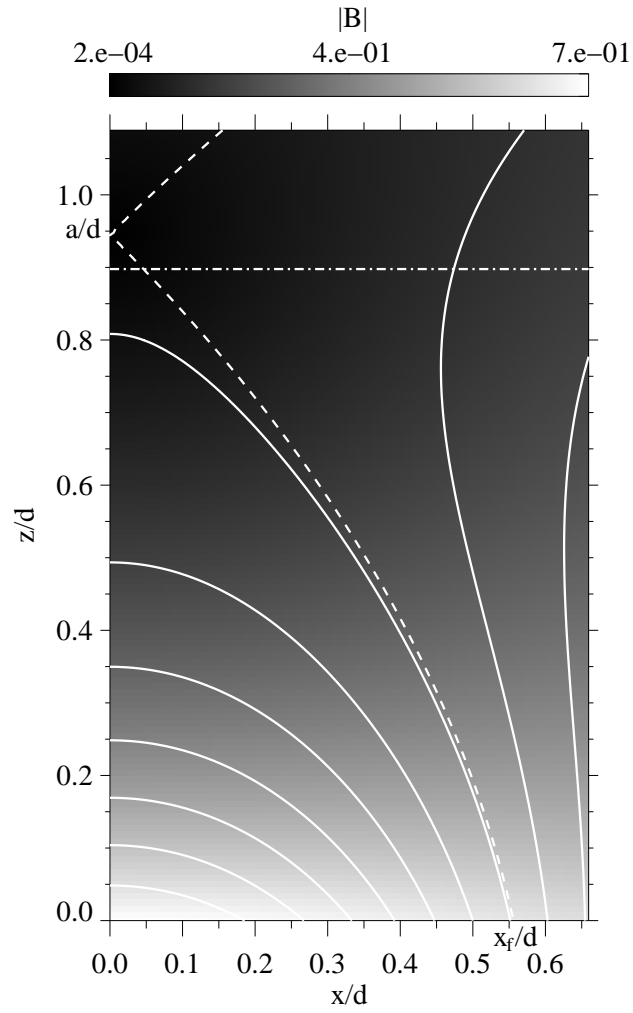


Fig. 1.— Magnetic field configuration (eq. (11)) with an aspect ratio  $R = a/x_f = 1.7$ . The white solid lines are the field lines, and the color contour is the field strength. The dashed line is the magnetic separatrix. The dash-dotted line is the upper boundary of the simulation domain.

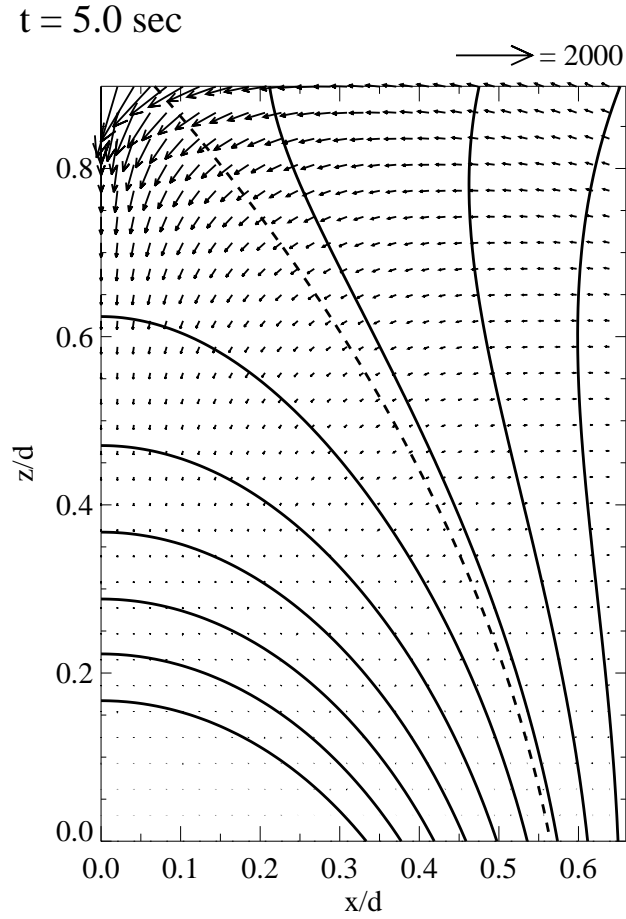


Fig. 2.—  $\mathbf{E} \times \mathbf{B}$  drift velocity field distribution calculated with eqs. (12), (13), and (17) at  $t = 5$  s. The unit of arrows is in  $\text{km s}^{-1}$ . The black lines are the magnetic field lines, and the dashed line is the magnetic separatrix.

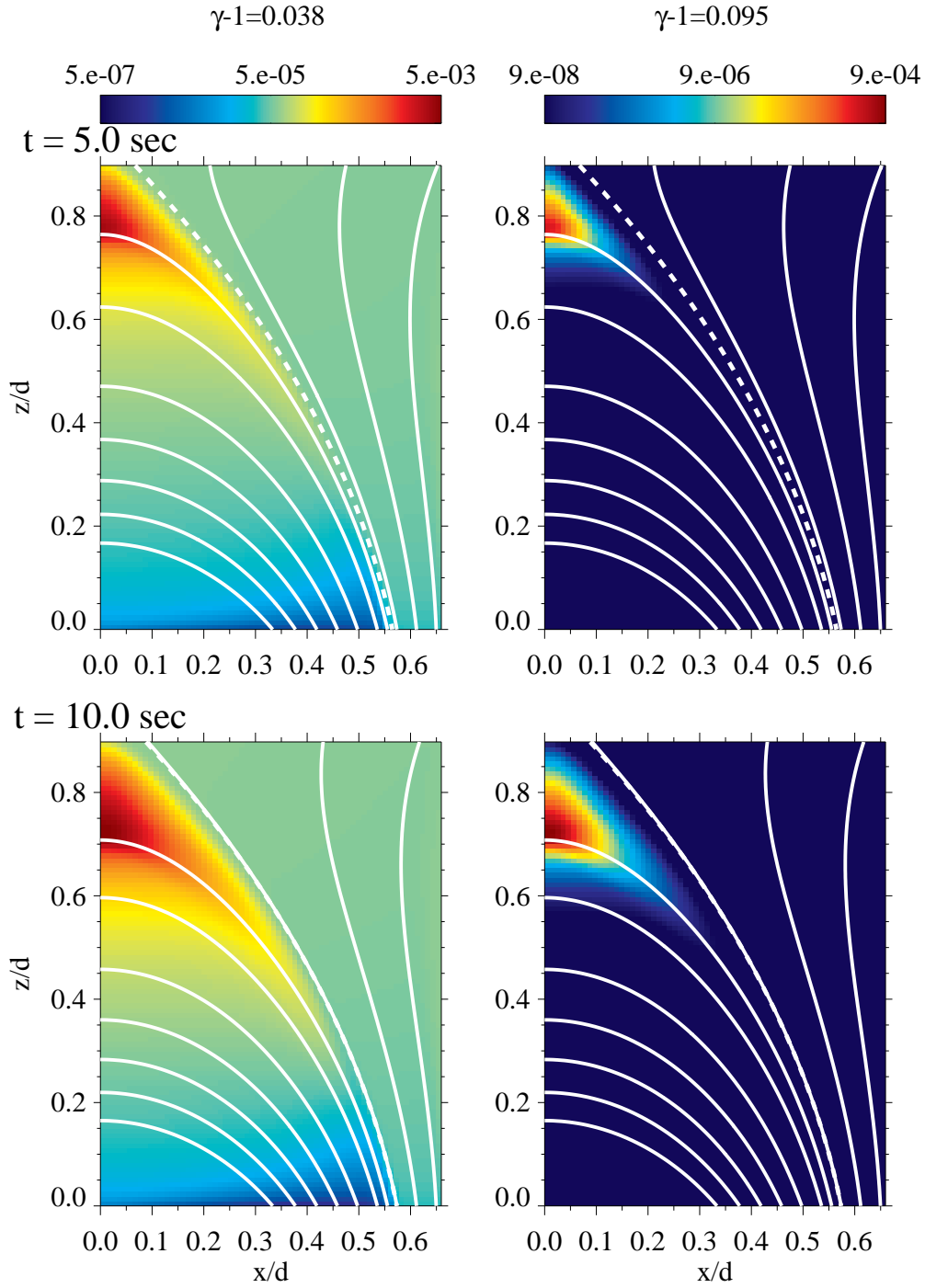


Fig. 3.— Spatial distribution of the number of 20 keV (left) and 50 keV (right) omnidirectional electrons at  $t = 5 \text{ s}$  (top) and  $10 \text{ s}$  (bottom). The white lines are the magnetic field lines, and the dashed lines are the magnetic separatrix.



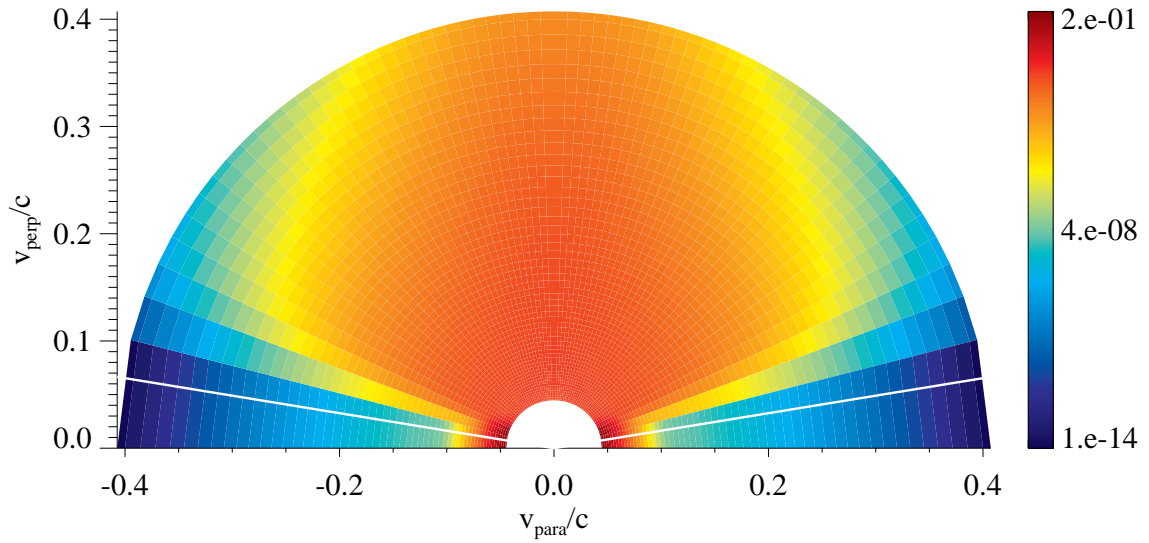


Fig. 4.— Velocity space distribution at  $(x, z) = (0, 0.7)$  at  $t = 10$  s, corresponding to the top of a closed loop. The horizontal and vertical axes correspond to the velocity parallel and perpendicular to the magnetic field line. The white lines denote the loss-cone angle.

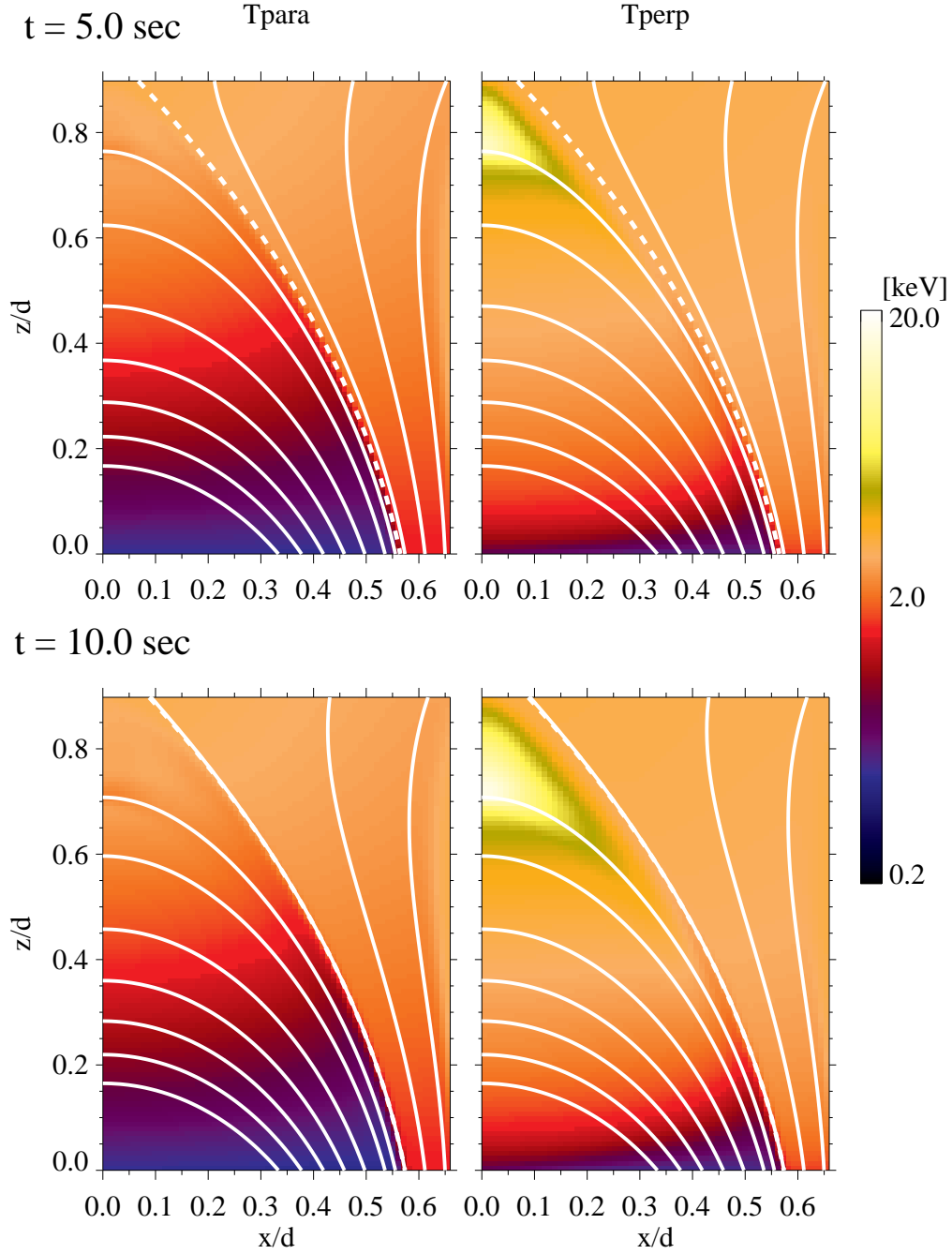


Fig. 5.— Spatial distribution of the parallel (left) and perpendicular (right) temperatures at  $t = 5 \text{ s}$  (top) and  $10 \text{ s}$  (bottom), calculated from eqs. (18) and (19). The white lines are the magnetic field lines, and the dashed lines are the magnetic separatrix.

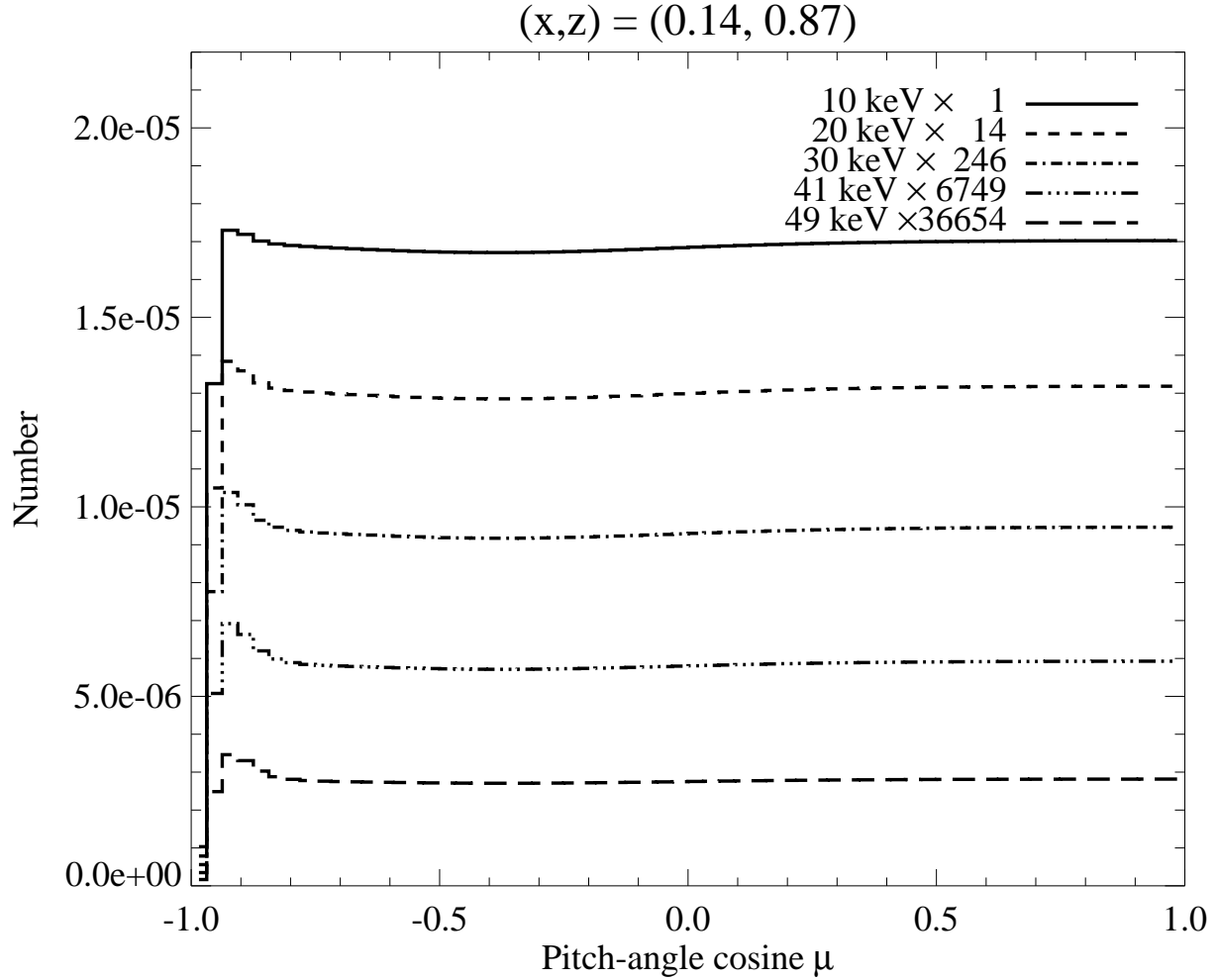


Fig. 6.— Electron pitch-angle distribution in the open field line near the magnetic separatrix  $(x, z) = (0.14, 0.87)$  at  $t = 5$  s. The positive (negative)  $\mu$  corresponds to the sunward (anti-sunward) direction. Different lines represent the electrons with different energies. Number density is multiplied by factors for illustration, as shown in the legend on the upper-right corner.

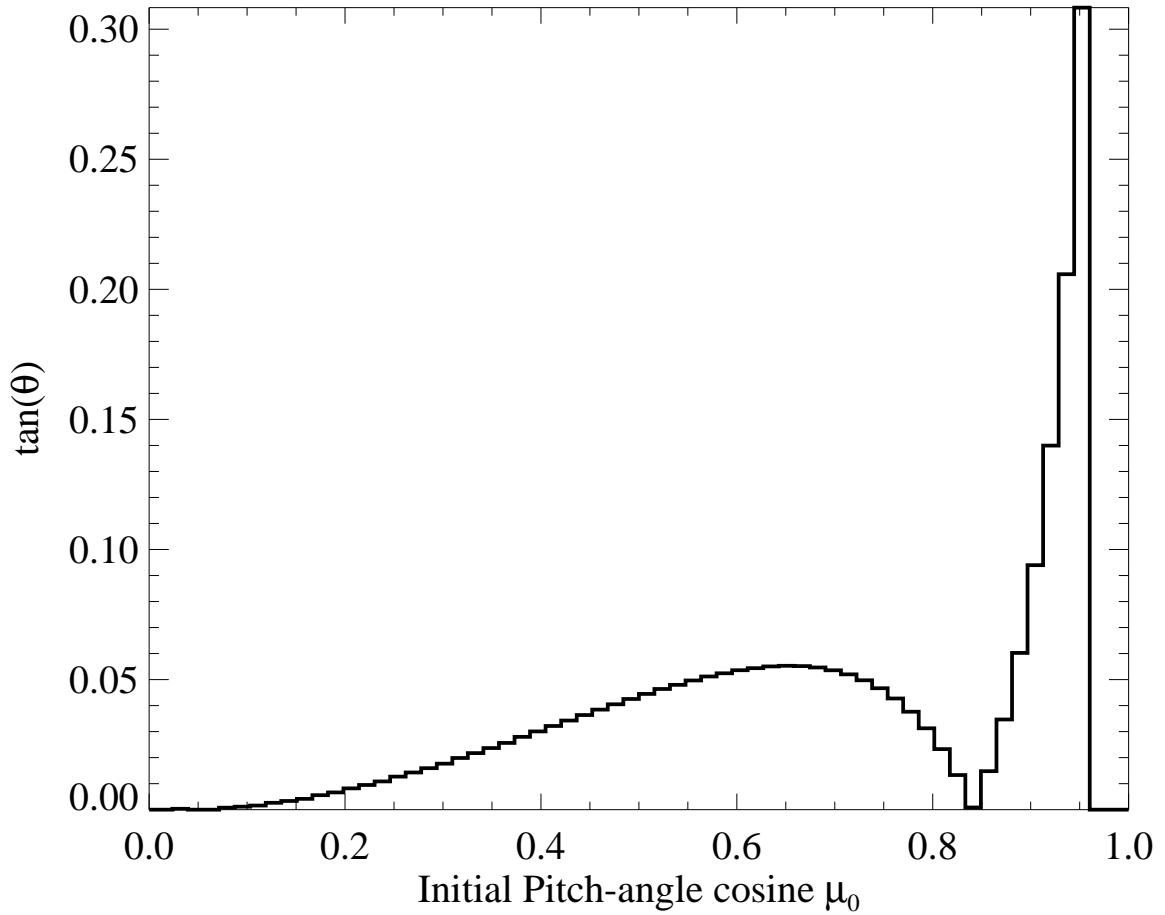


Fig. 7.— Tangent of an angle of the magnetic field line between the departure and mirror points of electrons, as a function of their initial pitch-angle cosine (see eqs. (30) and (31)), obtained from a test particle simulation with eqs. (7) - (9).

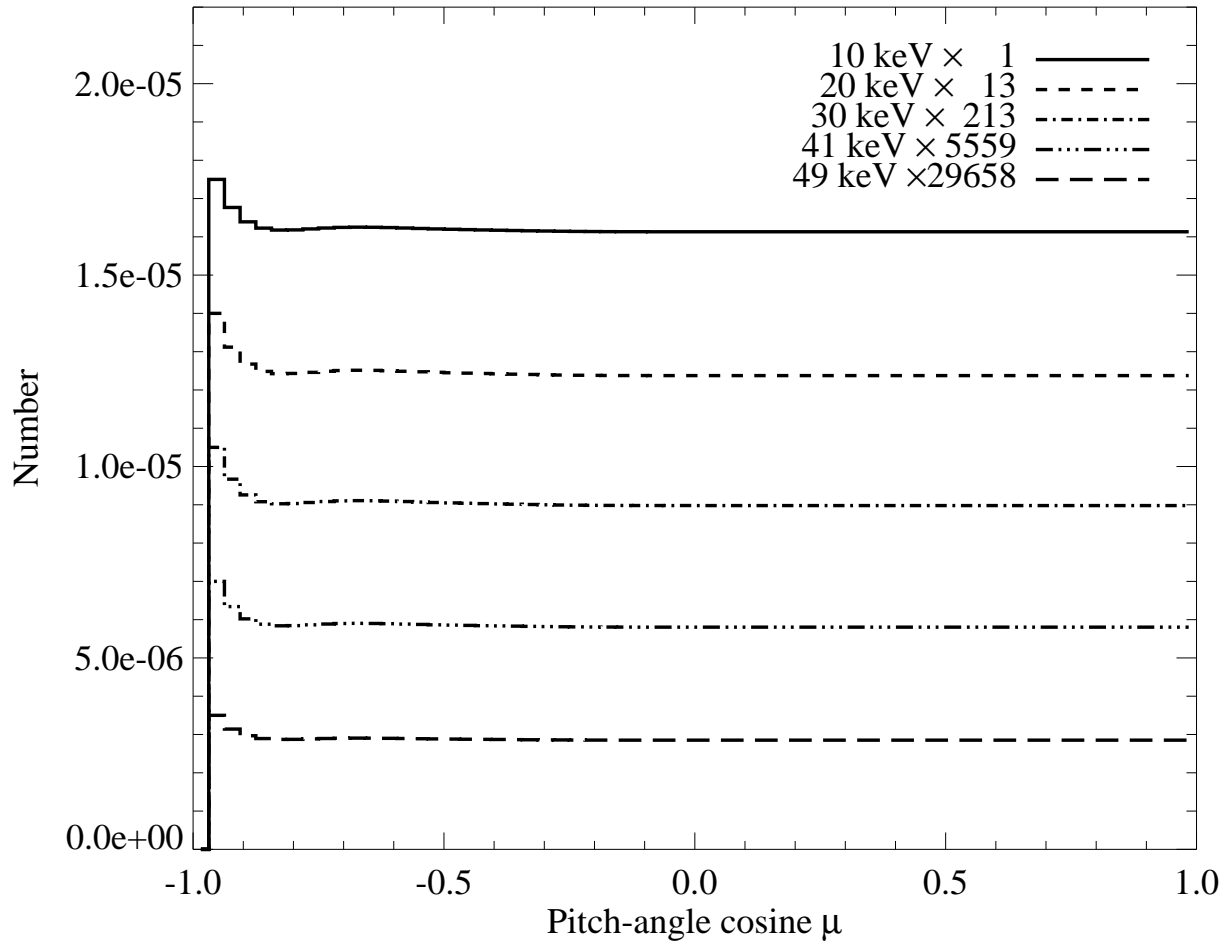


Fig. 8.— Electron pitch-angle distribution calculated from the analytic solution of eq. (29). The format of this Figure is same as of Figure 6.

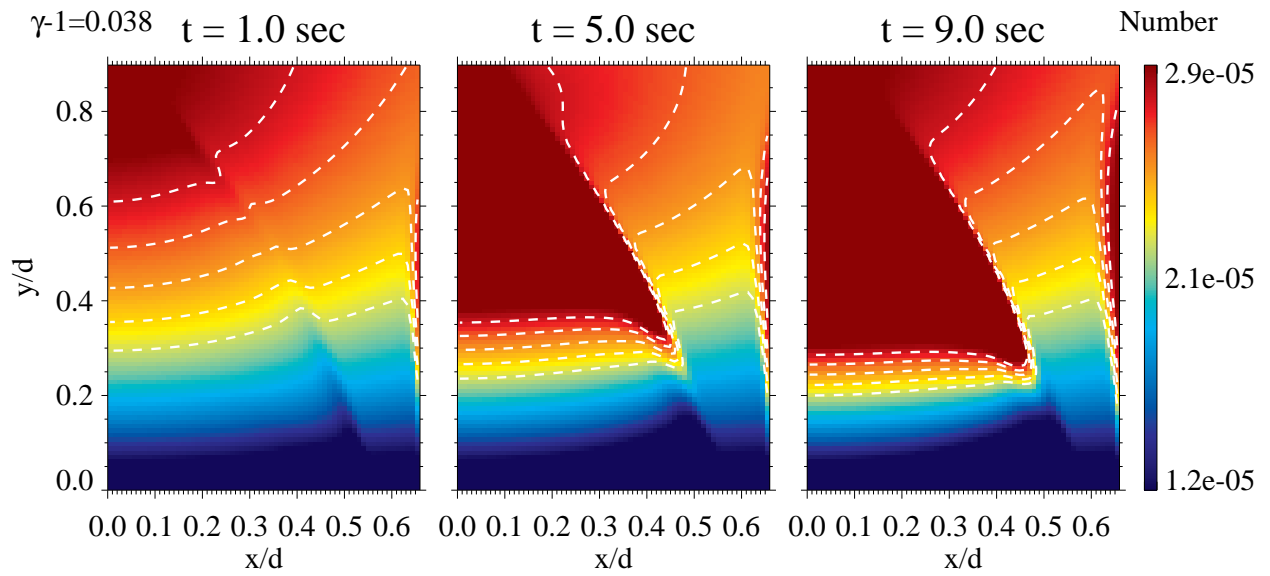


Fig. 9.— Spatial distribution of the number of 20 keV antisunward electrons at  $t = 1$  s (left), 5 s (center), and 9 s (right). The color scale is set so as to emphasize the gradient in open field lines (right-half area). The white dashed lines show the contours of the number of electrons, with levels of 75%, 80%, 85%, 90% and 95% of the maximum value.

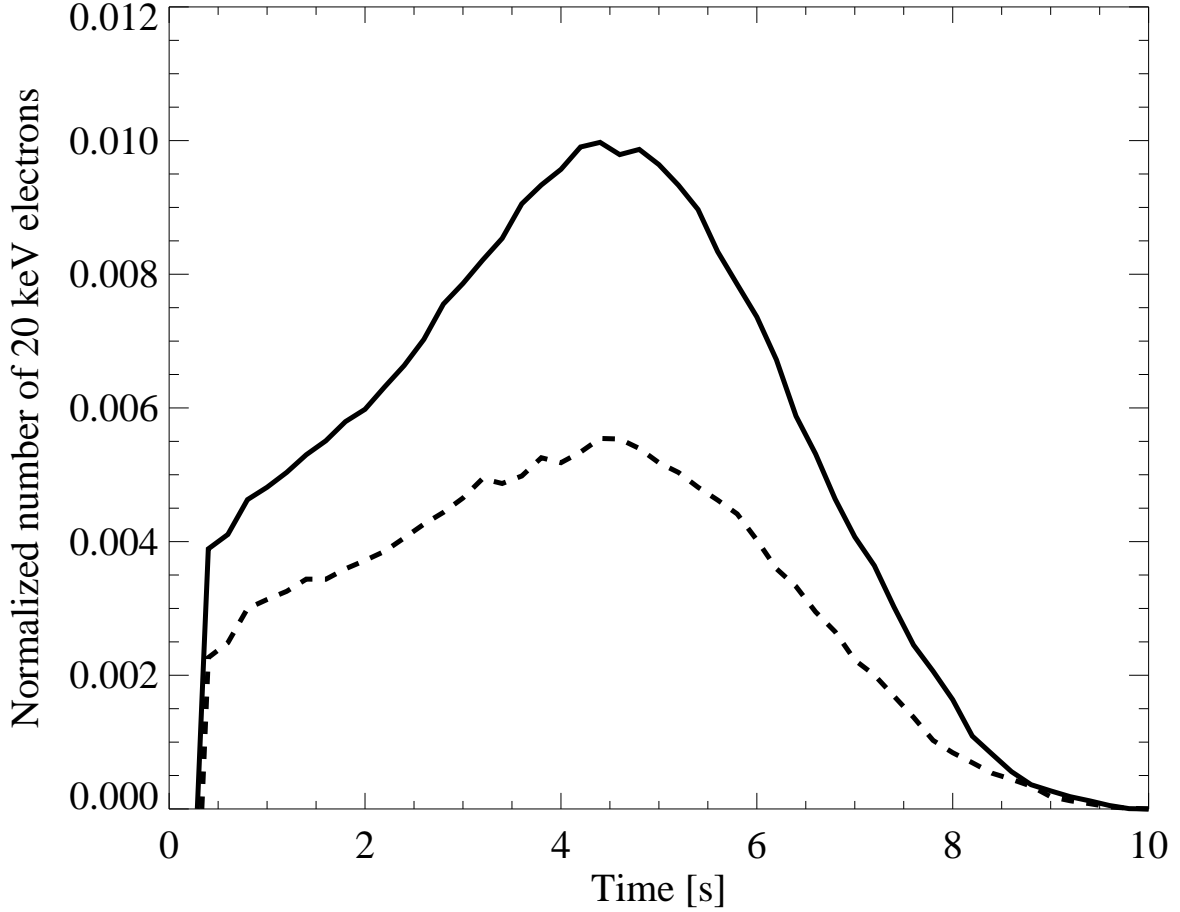


Fig. 10.— Time profile of the number of 20 keV escaping electrons (eq. (32)). The number is normalized to the initial distribution. The solid and dashed lines show the calculation results with  $v_p = 60$  and  $30 \text{ km s}^{-1}$ , respectively. Just after the start of the simulation, electrons initially in the loss cone are lost at the footpoint and the number of electrons drastically decreases, because the initial distribution is not a steady state solution in the model. This appears as the discontinuous jumps at  $t = 0.5 \text{ s}$ .

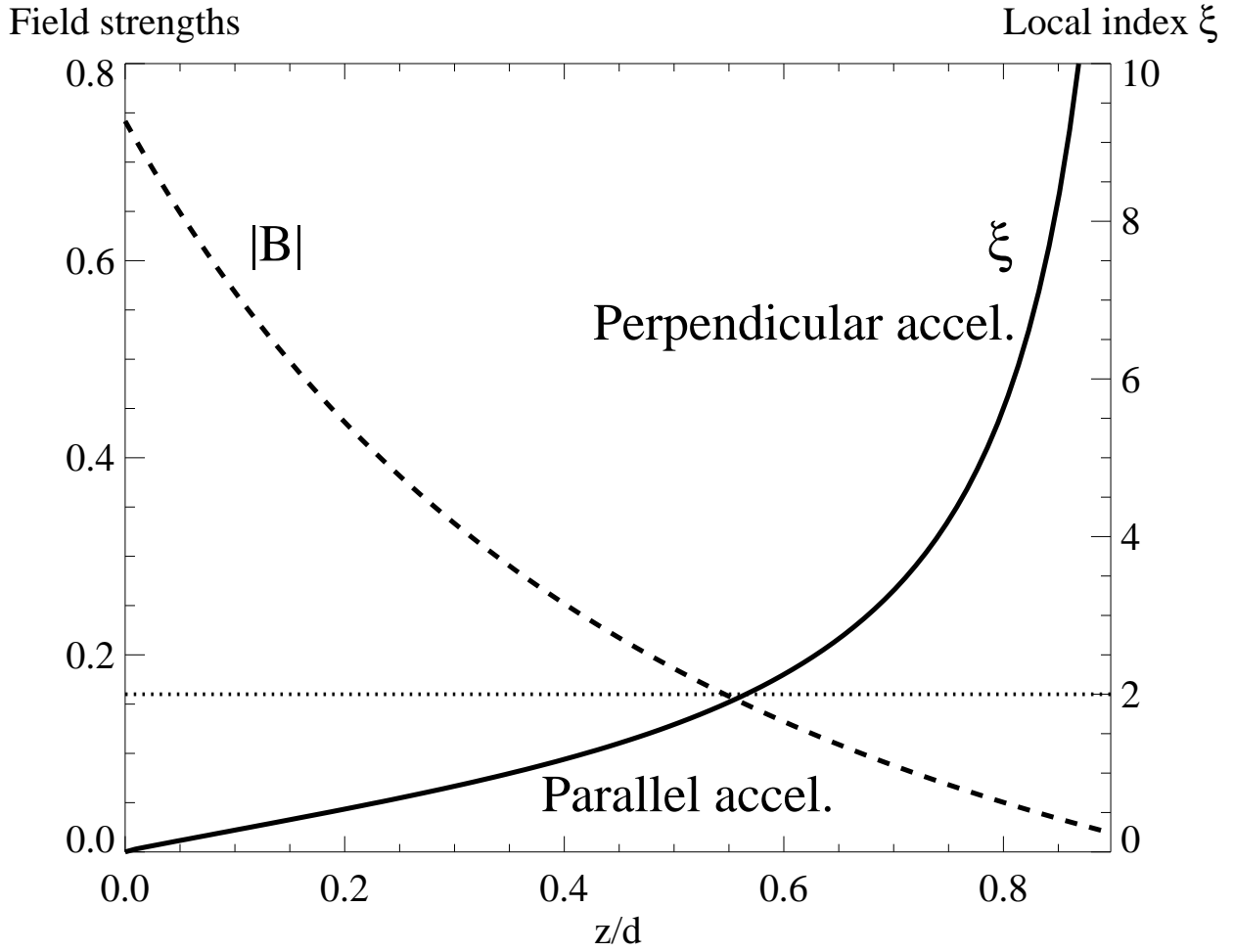


Fig. 11.— Strength of the model magnetic field (dashed line, eqs. (12) - (13)), and its local index  $\xi$  (solid line) at the apex of loops ( $x = 0$ ) at  $t = 5$  s, as a function of the altitude. It is expected from equation (33) that particles are accelerated more perpendicular (parallel) to the magnetic field line at which  $\xi$  is larger (smaller) than 2 (denoted as a dotted line).